Applied Ocean Research 108 (2021) 102524

Contents lists available at ScienceDirect

Applied Ocean Research

journal homepage: www.elsevier.com/locate/apor

Numerical simulation on flow characteristics of large-scale submarine mudflow

Yan Zhang [a,b], Xiaobing Lu [a,b], Xuhui Zhang [a,b,*], Peng Li [a,b]

[a] Institute of Mechanics, Chinese Academy of Sciences, Beijing 100190, China
[b] School of Engineering Science, University of Chinese Academy of Sciences, Beijing 100049, China

ARTICLE INFO

Keywords:
Submarine mudflow
Mass movement
Multiphase flow
Numerical simulation

ABSTRACT

Gas hydrate (GH) is widely distributed in the world according to the geological survey. Most of GH is located in the ocean. After GH dissociation, the strength of gas hydrate bearing sediments (GHBS) decreases accompanying the rise of pore pressure, which can cause marine landslide. Landslide may transform into mudflows during movement on the seabed. The massive movement of submarine mudflow can result in the serious deformation of (or even damage of) submarine pipelines, the dumping of offshore platforms, and tsunamis. In this paper, the flow characteristics of the large-scale submarine mudflow are investigated based on the Euler-Euler multiphase flow model combining with kinetic theory of granular flow (KTGF). The controlling dimensionless parameters, such as the initial depositional form and the relative depth, are given. The hydroplaning and frontal detachment during the mass movement are captured. The front velocity of the mudflow, and the free surface elevations at the sea level are analyzed. The numerical results show that the large-scale submarine mudflow has a significant impact on the sea level. The submarine mudflow should be taken into consideration during design of submarine pipelines and offshore platforms in GH-distributed sea area duo to its great destructive power.

1. Introduction

With the increase in worldwide energy demand, the exploitation of deep marine gas hydrate (GH), oil, and gas is of great concern. A significant amount of engineering infrastructures such as submarine pipelines have been constructed for the exploitation and transportation of the marine resources.

Most of GH is stored in the ocean bed. For example, the Shenhu area situated in the middle section of the northern slope of the South China Sea is rich in GH resource by geological survey (Li et al., 2010; Wang et al., 2014; Zhang et al., 2015; Zhang et al., 2020). GH dissociation can decrease the shear strength of gas hydrate bearing sediments (GHBS) by the decrease of the cohesion among sediment particles and rise of the excess pore pressure due to the released free gas (Jiang et al., 2015). The sediment containing GH is often semidiagenetic or not yet diagenetic and consists of clay, silt or sand, e.g. the soil type of GHBS in Shenhu area is silt with high water content according to experiments (Zhang et al., 2015). After GH dissociation, the GHBS and the over-layer can slide and easily transform into mudflow during movement on the seabed. The submarine mudflow is a process of sediment transporting from the shallow continental margin to the deeper parts of the ocean basin (De Blasio et al., 2004; Locat and Lee, 2002). Submarine mudflow can travel a long distance, hundreds of kilometers, even on very small slopes due to the effect of water softening and hydroplaning (Mohrig et al., 1998; Vanneste et al., 2014). A large-scale mass movement can result in serious deformation or rupture of oil and gas pipelines, the dumping of offshore platforms (Mosher et al., 2010), and can also generate destructive waves, even trigger a tsunami (Brune et al., 2010; Li et al., 2015; Terry et al., 2017). Therefore, it is of great importance to capture the main features of mass movement during a submarine mudflow, providing a reference for the layout of pipelines, and design of other engineering structures on the seabed. The GH dissociation is considered to be a significant factor causing submarine mudflow (Jiang et al., 2015; Lu et al., 2017; Chen et al., 2020), such as the large-scale slides at Cape Fear in North Carolina (Cashman and Popenoe, 1985) and Blake Ridge off the southeastern coast of the U.S. (Dillon et al., 1998).

The current field data and understanding of submarine mudflow are insufficient, the researchconcerning submarine mudflows mainly focus on small-scale model experiments and numerical simulations. Mohrig et al. (1999) designed a “Fish Tank” of 10 m long, 3 m high and 0.6 m wide, containing a rectangular channel with an inner width of 0.2 m and

* Corresponding author.
E-mail addresses: zhangyan162@imech.ac.cn (Y. Zhang), xblu@imech.ac.cn (X. Lu), zhangxuhui@imech.ac.cn (X. Zhang), lipeng@imech.ac.cn (P. Li).

https://doi.org/10.1016/j.apor.2021.102524
Received 19 August 2020; Received in revised form 21 December 2020; Accepted 31 December 2020
Available online 27 January 2021

transparent vertical walls. The subaqueous and subaerial debris flows were simulated and compared. The results indicated that subaqueous debris flows can move farther due to hydroplaning. Zakeri (2009) and Zhang et al. (2019) studied the impact of submarine debris flow on marine pipelines, and put forward an empirical formula. Guo et al. (2019) used a low-temperature Herschel-Bulkley rheological model to describe the submarine mudflows, which is considered as a mixture of the seawater and sediments. The runout of submarine landslide was investigated by using the material point method and the particle method (Dong et al., 2017; Qiu et al., 2017). Recently, the theory of multiphase flow has been applied to understand the submarine mudflow mass movement (SMMM). A small-scale submarine mudflow was simulated, and the model was validated by Gauer et al. (2006). The forces due to submarine debris flows on pipelines were obtained, and the relationship between the drag coefficient and the Reynolds number was given (Zakeri et al., 2009). Abbas et al. (2011) used the Euler-Euler two-phase flow model to describe sediment transport processes and simulate the tunnel erosion beneath marine pipelines. Xiu et al. (2015, 2016) analyzed the development of submarine mudflow by adopting the Euler-Euler two-phase flow model. The simulation can capture some features of the actual submarine mudflow and reproduce the mass movement process. Yu and Lee (2019) employed a rheology-based multi-phase flow model to study a small-scale underwater landslide on the inclined planes where the effects of particle size and the rough bed condition was considered. Lee (2019) applied the rheology-based multiphase flow model to simulate a large scale submarine mudflow with considering the turbulent motions of fluid and particles.

The mass movement of small-scale submarine mudflow is well understood. Small-scale experiments and numerical simulations only provide some qualitative analysis. Nevertheless, only a little attention has been devoted to the mechanical characteristics of large-scale submarine mudflow and the impact of the submarine mudflow on the sea level. There is a high probability that the submarine mudflow occurs due to GH dissociation in the seabed located at the continental slope, e.g. Shenhu area due to the geotechnical physical properties.

We investigate the flow characteristics of large-scale SMMM by using the mechanical properties of GHBS in Shenhu area, South China Sea based on the Euler-Euler multiphase flow model combining with kinetic theory of granular flow (KTGF). In Section 2, the numerical model is presented, and the dimensional analysis of the problem is processed to obtain the controlling dimensionless parameters. In Section 3, the effects of the dimensionless parameters on the mass movement and sea level are simulated and discussed.

2. Methodology

2.1. Model description

The SMMM is a mixture of the sediment particles and the seawater moving on the slope, which is a typical two-phase flow process and can be considered as granular flow. The Euler-Euler multiphase flow model is adopted to describe the SMMM. The seawater, and the sediments after GH dissociation constitute a two-phase system. To capture the free surface elevations on the sea level, a phase air is added above the seawater. The mass conservation equations for the three phases can be written as

$$\frac{\partial}{\partial t}(\alpha_q \rho_q) + \nabla\cdot(\alpha_q \rho_q \mathbf{U}_q) = 0, \tag{1}$$

where α_q, ρ_q and $\mathbf{U}_q$ are the volume fraction, density and the velocity for each phase, respectively; ∇ is the gradient operator. The volume fractions of the three phases satisfy the following condition: $\alpha_w + \alpha_s + \alpha_a = 1$. Actually, there only be two phases at any position because the sediment phase will not contact with the air phase, which can be called a pseudo three-phase flow.

The momentum conservation equations for the three phases are:

$$\frac{\partial}{\partial t}(\alpha_w \rho_w \mathbf{U}_w) + \nabla\cdot(\alpha_w \rho_w \mathbf{U}_w \mathbf{U}_w) = -\alpha_w \nabla P + \nabla\cdot\boldsymbol{\tau}_w + \alpha_w \rho_w \mathbf{g} + K_{ws}(\mathbf{U}_w - \mathbf{U}_s), \tag{2}$$

$$\frac{\partial}{\partial t}(\alpha_s \rho_s \mathbf{U}_s) + \nabla\cdot(\alpha_s \rho_s \mathbf{U}_s \mathbf{U}_s) = -\alpha_s \nabla P - \nabla P_s + \nabla\cdot\boldsymbol{\tau}_s + \alpha_s \rho_s \mathbf{g} + K_{sw}(\mathbf{U}_s - \mathbf{U}_w), \tag{3}$$

$$\frac{\partial}{\partial t}(\alpha_a \rho_a \mathbf{U}_a) + \nabla\cdot(\alpha_a \rho_a \mathbf{U}_a \mathbf{U}_a) = -\alpha_a \nabla P + \nabla\cdot\boldsymbol{\tau}_a + \alpha_a \rho_a \mathbf{g}, \tag{4}$$

where P is the three-phase pressure, P_s is the sediment phase pressure, $\mathbf{g}$ is the gravity acceleration, $K_{ws} = K_{sw}$ are the momentum exchange coefficients between the seawater phase and sediment phase, $\boldsymbol{\tau}_w$, $\boldsymbol{\tau}_a$ and $\boldsymbol{\tau}_s$ are the stress tensor of the seawater phase, air phase, and sediment phase, respectively. The interaction force model proposed by Gidaspow (1994) is used. The momentum exchange coefficient is expressed as:

$$K_{sw} = \begin{cases} \frac{3}{4} C_D \frac{\alpha_s(1-\alpha_s)\rho_w|\mathbf{U}_s - \mathbf{U}_w|}{d_s}\alpha_w^{-2.65}, & \alpha_w \geq 0.8 \\ 150\frac{\alpha_s(1-\alpha_w)\mu_w}{\alpha_w d_s^2} + 1.75\frac{\rho_w \alpha_s|\mathbf{U}_s - \mathbf{U}_w|}{d_s}, & \alpha_w < 0.8 \end{cases}, \tag{5}$$

$$C_D = \begin{cases} \frac{24(1+0.15Re^{0.687})}{Re}, & Re \leq 1000 \\ 0.44, & Re > 1000 \end{cases}, \tag{6}$$

$$Re = \frac{\rho_w|\mathbf{U}_s - \mathbf{U}_w|d_s}{\mu_w}, \tag{7}$$

where C_D is the drag coefficient, Re is the relative Reynolds number, μ_w is the shear viscosity of the seawater, and d_s is the diameter of the sediment particles. The stress tensor of the seawater phase and air phase are expressed as:

$$\boldsymbol{\tau}_w = \alpha_w \mu_w\left(\nabla\mathbf{U}_w + \nabla\mathbf{U}_w^T\right) + \frac{2}{3}\alpha_w \mu_w \nabla\cdot\mathbf{U}_w\mathbf{I}, \tag{8}$$

$$\boldsymbol{\tau}_a = \alpha_a \mu_a\left(\nabla\mathbf{U}_a + \nabla\mathbf{U}_a^T\right) + \frac{2}{3}\alpha_a \mu_a \nabla\cdot\mathbf{U}_a\mathbf{I}, \tag{9}$$

where μ_w and μ_a are the shear viscosity of the seawater and air. The sediment stress in the KTGF in the present paper is based on a kinetic-collisional-frictional law, which is different from the conventional kinetic-theory based model and can be applied to dense granular flows. This model combines the frictional model with the conventional kinetic-theory based model to deal with the quasi-static regime in which the enduring inter-particle contacts are predominant. Si et al. (2018) point that a generally valid constitutive relation for the sediment phase should cover two distinct regimes: the collisional regime and the quasi-static regime and he used a similar two-phase model to simulate the submarine granular flows. The sediment stress $\boldsymbol{\tau}_s$ and sediment pressure P_s is written as

$$\tau_s = \boldsymbol{\tau}_s^{k,c} + \boldsymbol{\tau}_s^{f}, \tag{10}$$

$$P_s = P_s^{k,c} + P_s^{f}, \tag{11}$$

where $\boldsymbol{\tau}_s^{k,c}$ and $P_s^{k,c}$ are the kinetic and collisional components of the sediment stress and sediment pressure, respectively. The two components are used for the collisional regime (Si et al., 2018). $\boldsymbol{\tau}_s^{f}$ and P_s^{f} are the frictional components due to enduring contacts in the frictional regime, which depends closely on the volume fraction of the sediment particles. The kinetic and collisional stress ($\boldsymbol{\tau}_s^{k,c}$) is written as

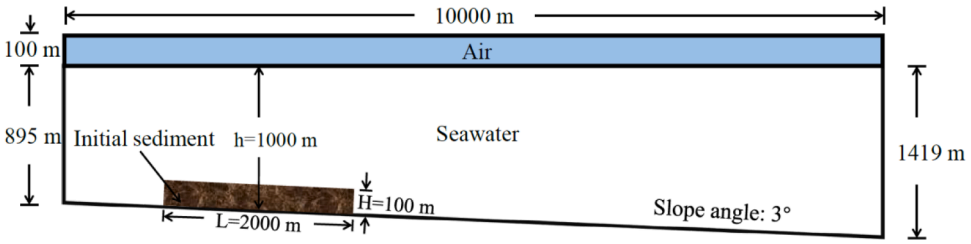

Fig. 1. Geometry of the standard case: the sediments are initially deposited on the slope, which is assumed as a rectangular. The surrounding medium is the seawater. The air is above the seawater.

$$\boldsymbol{\tau}_s^{k,c} = \alpha_s \mu_s^{k,c}\left(\nabla \mathbf{U}_s + \nabla \mathbf{U}_s^T\right) + \frac{2}{3}\alpha_s\left(\lambda_s - \frac{2}{3}\mu_s^{k,c}\right)\nabla\cdot\mathbf{U}_s\mathbf{I}, \tag{12}$$

where $\mu_s^{k,c} = \mu_s^k + \mu_s^c$ is the sum of the kinetic viscosity (μ_s^k) and collisional viscosity (μ_s^c) of the sediment phase, λ_s is the bulk viscosity of the sediment phase, and $\mathbf{I}$ is the unit tensor. The frictional stress ($\boldsymbol{\tau}_s^f$) is also written in Newtonian form

$$\boldsymbol{\tau}_s^f = \alpha_s \mu_s^f\left(\nabla \mathbf{U}_s + \nabla \mathbf{U}_s^T\right), \tag{13}$$

where μ_s^f is the frictional viscosity and is expressed as (Schaeffer, 1987)

$$\mu_s^f = \frac{P_s^f sin\varphi}{2\sqrt{I_{2D}}}, \tag{14}$$

where I_{2D} is the second invariant of the deviatoric sediment phase frictional stress tensor. Considering that the frictional pressure vanishes under the loosely packed condition, the following expression is used in this paper (Johnson and Jackson, 1987)

$$P_s^f = \begin{cases} 0, & \alpha_s < \alpha_{s,min} \\ Fr\dfrac{(\alpha_s - \alpha_{s,min})^n}{(\alpha_{s,max} - \alpha_s)^p}, & \alpha_{s,min} \le \alpha_s \le \alpha_{s,max} \end{cases}, \tag{15}$$

where coefficient $Fr = 0.05$, $n = 3$, $p = 5$ (Cheng et al., 2017), $\alpha_{s,min}$ is the loosely packed volume fraction, and $\alpha_{s,max}$ is the closely packed volume fraction. $\alpha_{s,min}$ and $\alpha_{s,max}$ are set as 0.50 and 0.63, respectively.

Based on the KTGF method, an additional equation, i.e. the particle temperature equation, is solved to represent the fluctuations brought by the sediment particles. The fluctuations represent the kinetic energy of the random motion of the sediment particles. The particle temperature equation is written as (Ding and Gidaspow, 1990):

$$\frac{3}{2}\left[\frac{\partial}{\partial t}(\rho_s\alpha_s\Theta_s) + \nabla\cdot(\rho_s\alpha_s\mathbf{U}_s\Theta_s)\right] = (-P_s\mathbf{I} + \boldsymbol{\tau}_s) : \nabla\mathbf{U}_s + \nabla\cdot(k_{\Theta s}\nabla\Theta_s) - \gamma_{\Theta s} + \Phi_{ws}, \tag{16}$$

where Θ_s is the temperature, $k_{\Theta s}$ is the diffusion coefficient of the sediment particles energy, $\gamma_{\Theta s}$ is the collision dissipation of energy, and $\Phi_{ws} = -3K_{ws}\Theta_s$ is the energy exchange between the seawater phase and sediment phase.

The kinetic and collisional components of the sediment phase pressure can be evaluated as (Lun et al., 1984):

$$P_s = \alpha_s\rho_s\Theta_s + 2\rho_s(1+e)\alpha_s^2 g_0\Theta_s, \tag{17}$$

where e is the particle-particle restitution coefficient which is set as 0.9, g_0 is the radial distribution function, $\alpha_s\rho_s\Theta_s$ is the kinetic contribution, and $2\rho_s(1+e)\alpha_s^2 g_0\Theta_s$ is the collisional contribution.

The radial distribution function is written as (Ogawa et al., 1980):

$$g_0 = \left[1 - \left(\frac{\alpha_s}{\alpha_{s,max}}\right)^{\frac{1}{3}}\right]^{-1}. \tag{18}$$

The collision dissipation of energy (Lun et al., 1984) and the diffusion coefficient of the sediment particle temperature (Gidaspow et al., 1991) are expressed as:

$$\gamma_{\Theta s} = \frac{12(1-e^2)g_0}{d_s\sqrt{\pi}}\rho_s\alpha_s^2\Theta_s^{\frac{3}{2}}, \tag{19}$$

$$k_{\Theta s} = \frac{25\rho_s d_s\sqrt{\Theta_s\pi}}{64(1+e)g_0}\left[1 + \frac{6}{5}\alpha_s g_0(1+e)\right]^2 + 2\rho_s\alpha_s^2 d_s(1+e)g_0\sqrt{\frac{\Theta_s}{\pi}}. \tag{20}$$

The kinetic viscosity (μ_s^k) is from the Syamlal model (Syamlal et al., 1993), and the collisional viscosity (μ_s^c) is from the Gidaspow model (Gidaspow, 1994):

$$\mu_s^k = \frac{\alpha_s\rho_s d_s\sqrt{\Theta_s\pi}}{6(3-e)}\left[1 + \frac{2}{5}(1+e)(3e-1)\alpha_s g_0\right], \tag{21}$$

$$\mu_s^c = \frac{4}{5}\alpha_s^2\rho_s d_s g_0(1+e)\sqrt{\frac{\Theta_s}{\pi}}, \tag{22}$$

$$\lambda_s = \frac{4}{3}\alpha_s^2\rho_s d_s g_0(1+e)\sqrt{\frac{\Theta_s}{\pi}}, \tag{23}$$

where φ is the angle of internal friction which is taken as 3° (Zhang et al., 2015).

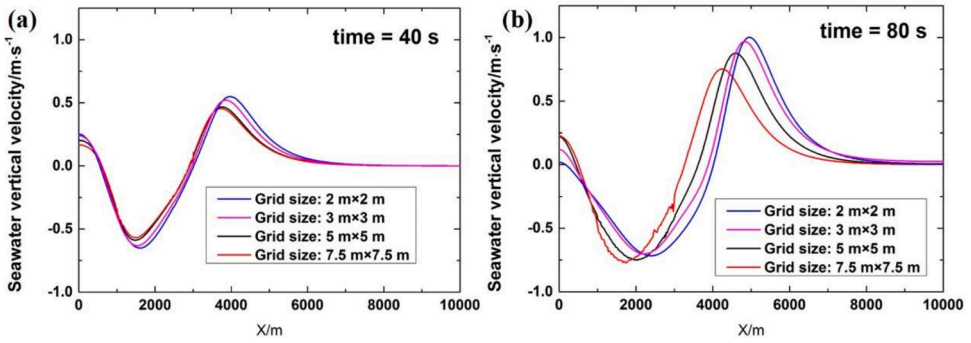

Fig. 2. Comparison of the seawater vertical velocity on the sea level with different grid size, at time = (a) 40 s, and (b) 80 s. (Standard Case)

2.2. Geometry and mesh

In order to simplify the numerical simulation, it is assumed that the sediment deposit shape at the initial moment is rectangular with height H and length L. The vertical distance from the midpoint of the bottom of the rectangular sediment to the sea level is defined as the seawater depth h. In the numerical simulation, a standard case is first calculated, with H=100 m, L=2000 m, h=1000 m, slope angle $\theta = 3°$, seawater density $\rho_w = 1000$ kg/m^3, seawater viscosity $\mu_w = 1.0 \times 10^{-3}$ Pa•s, air density 1.22 kg/m^3, and air viscosity 1.79×10^{-5} Pa•s. Subsequent analyses on the effects of the parameters are based on this case. Fig. 1 shows the model of the standard case. To evaluate the mesh independence, we perform numerical simulations with 4 different grid sizes (2 m × 2 m, 3 m × 3 m, 5 m × 5 m, and 7.5 m × 7.5 m). By comparing the results, we find that the seawater vertical velocity at the sea level in the simulation with grid size 3 m × 3 m is similar to that with grid size 2 m × 2 m (Fig. 2). The grid size is taken as 3 m × 3 m. The time step is set as 0.001 s.

2.3. Initial and boundary conditions

At the initial moment, the sediments are static on the slope. The sediments are considered between the closely packed condition and loosely packed condition. The volume fraction of the sediments is set as 0.6. The left and right side of the model are set as the free slip wall boundary conditions for the three phases. The seabed is set as no slip. The top is set as the pressure outlet boundary condition. The phase coupled simple method is used for the pressure-velocity coupling. The gradient is discretized by the Green-Gauss cell based method. The momentum equation is treated with second order upwind scheme. ANSYS FLUENT software is used for the simulation.

2.4. Dimensional analysis

Dimensional analysis is conducted to obtain the controlling parameters of the SMMM in this paper. The parameters in the numerical simulation include the initial depositional length L and height H of the sediments, the seawater depth h, the sediment density ρ_s, the sediment particle diameter d_s, the density ρ_w and viscosity μ_w of the seawater, the gravity acceleration g, and the slope angle θ. The front velocity (U) of the sediments can be expressed as:

$$U = f(h, H, L, \rho_s, d_s, \rho_w, \mu_w, g, \theta, t). \tag{24}$$

Choosing ρ_w, g, and L to normalize Eq.(24) goes here yields (Tan, 2011):

$$U^* = f\left(\frac{H}{L}, \frac{h}{L}, \frac{d_s}{L}, \frac{\rho_s}{\rho_w}, \frac{g d_s^3 \rho_w^2}{\mu_w^2}, \theta, T\right), \tag{25}$$

where $U^* = U/\sqrt{gL}$ is the non-dimensional front velocity, H/L represents the initial depositional form, h/L is the relative depth of sediments on the seabed, ρ_s/ρ_w is the ratio of density between the sediments and the seawater, $g d_s^3 \rho_w^2/\mu_w^2$ is the Archimedes number which represents the settling effect of the sediment particles, and $T = t/\sqrt{L/g}$ is the dimensionless flow time.

The seawater density ρ_w, viscosity μ_w, the sediment density ρ_s, and sediment particle diameter d_s are regarded as constant. Then, Eq. (25) can be rewritten as:

$$U^* = f\left(\frac{d_s}{L}, \frac{H}{L}, \frac{h}{L}, \theta, T\right). \tag{26}$$

Then the effects of above dimensionless numbers H/L, h/L, and θ on the flow characteristics of a large-scale SMMM are investigated.

The properties of the sediment samples retrieved from Shenhu area, South China Sea were tested by Zhang et al. (2015). The particle size distribution curve and cumulative particle size distribution curve of the sediment are given in Fig. 3, which shows that sediment is generally silt. The specific weight of the sediment is about 2.75. The average diameter of the sediment particles is about 0.02 mm which is adopted as the particle size less than 50% of the total soil weight. With this particle size, it is cohesive sediments. However, based on the experiments on the strength of the sediments after hydrate dissociation (Zhang et al., 2015), the cohesion strength and the internal friction angle are 3-6 kPa and 0.5-5°, respectively. The cohesion of the sediments after hydrate dissociation is very small. The ratio of drag force strength (S_D) to cohesion strength (S_C) is

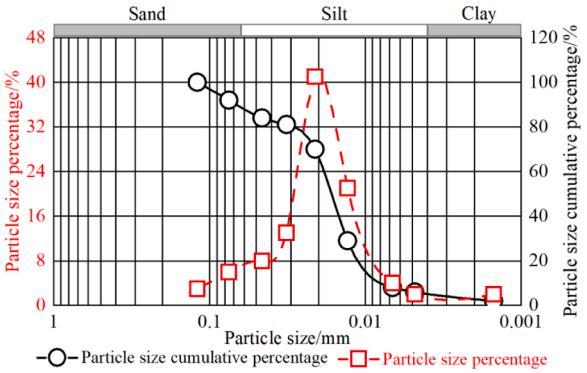

Fig. 3. The sediment particle size distribution curve in Shenhu area, South China Sea.

Table 1
List of the value range of parameters in the Shenhu area, South China Sea.

Parameters	Reported range in literature	References
H	50 – 300 m	Li et al. (2010), Wu et al. (2011), Wang et al. (2014), Wang et al. (2011), Su et al. (2012)
h	800 – 1700 m	Li et al. (2010), Zhang et al. (2017)
θ	0 – 10°	Liu et al. (2010)

$$\frac{S_D}{S_C} = \frac{\left(150\frac{\alpha_s(1-\alpha_w)\mu_w}{\alpha_w d_s^2} + 1.75\frac{\rho_w \alpha_s |\mathbf{U}_s - \mathbf{U}_w|}{d_s}\right)\cdot|\mathbf{U}_s - \mathbf{U}_w| d_s}{c} \approx 1.2, \tag{27}$$

with $|\mathbf{U}_s - \mathbf{U}_w| = 1$ m/s, and $\alpha_s = 0.5$, which is close to the initial condition of the sediments. This means that when the sediment particles start to move under gravity and the velocity reaches 1 m/s, the particles will be pulled apart by the water and become loose. When the mudflow reaches the inertial state with the sediment particles move freely and they instantaneously collide with each other (Lee et al., 2015), the velocity will be the order of tens or even hundreds (Lee, 2019). The ratio of drag strength to cohesion strength is about 200 at this state. Hence, the soil cohesion is not considered in this paper.

The value range of other parameters in Shenhu area are shown in Table 1. All the cases for numerical simulation are given in Table 2. The density and the viscosity of the air are 1.22 kg/m^3 and 1.79×10^{-5} Pa•s, respectively. The bold part is the standard case. Case 1-5 are designed to study the effect of the initial depositional form (H/L). Case 2, 6, 7, 8, and 9 are designed to study the effect of the relative depth (h/L). Case 2, 10, and 11 are concerning the effect of the slope angle (θ).

3. Results and discussion

3.1. Model verification

Haza et al. (2013) conducted an experiment by generating the mudflow on a slope to observe the flow structures of the mudflow. The

Table 2
Parameters in the numerical simulation.

Case	Initial depositional size			Sediment phase		Seawater phase		Dimensionless numbers		
	H/m	L/m	h/m	ρ_s/kg·m^{-3}	d_s/mm	ρ_w/kg·m^{-3}	μ_w/ Pa·s	H/L	h/L	θ
1	50	2000	1000	2750	0.02	1000	0.001	0.025	0.5	3°
2	**100**	**2000**	**1000**	**2750**	**0.02**	**1000**	**0.001**	**0.050**	**0.5**	**3°**
3	150	2000	1000	2750	0.02	1000	0.001	0.075	0.5	3°
4	200	2000	1000	2750	0.02	1000	0.001	0.100	0.5	3°
5	250	2000	1000	2750	0.02	1000	0.001	0.125	0.5	3°
6	100	2000	800	2750	0.02	1000	0.001	0.050	0.4	3°
7	100	2000	1200	2750	0.02	1000	0.001	0.050	0.6	3°
8	100	2000	1400	2750	0.02	1000	0.001	0.050	0.7	3°
9	100	2000	1600	2750	0.02	1000	0.001	0.050	0.8	3°
10	100	2000	1000	2750	0.02	1000	0.001	0.050	0.5	1°
11	100	2000	1000	2750	0.02	1000	0.001	0.050	0.5	5°

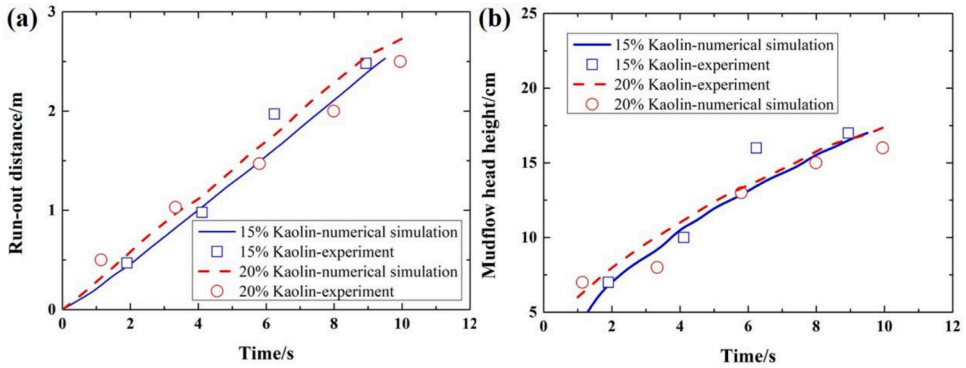

Fig. 4. Comparison of the mudflow in water between the numerical simulation results and the experimental data, (a) run-out distance, and (b) mudflow head height.

mud in the experiment was a mixture of Kaolin and water with the Kaolin mass percentage change from 10% to 35%. The density of the Kaolin and the water are 2630 kg/m^3 and 1000 kg/m^3, respectively. The diameter of the Kaolin is about 0.008 mm and the slope angle is 3°. Fig. 4 gives the comparison of the run-out distance and the mudflow head height with timeline feature.

Grilli et al. (2017) carried out laboratory experiments for simulation of submarine mass failures by letting glass beads move down a plane slope. The experiment of Grilli et al. (2017) is used to verify the Euler-Euler multiphase flow model in Section 2.1. In their experiments, a mass of glass beads with density 2500 kg/m^3 and diameter 4 mm is deposited in a triangular shape box full of water. The density of water is 1000 kg/m^3. The triangular box is located on a slope with a slope angle 35°. A high-speed video camera (at 1000 frames per second) is used to record the underwater motion of the glass beads on the slope. Fig. 5 shows the comparison of the slide cross sections between the numerical simulation results and the experimental image. Fig. 6 gives the comparison of the stacking height of the glass beads between the numerical simulation results and the experimental data. Fig. 7 shows the comparison of the time series of free surface elevations between the numerical simulation results and the experimental data at two wave gages in experiments of Grilli et al. (2017). It can be found that the movement distance of the glass beads is slightly smaller than the experimental value, and the stacking height is slightly larger than the experimental value. The error may be due to the difference between the initial volume fraction of the glass beads in the numerical simulation and the experimental value, which resulting in large resistance on the glass beads. The friction angle of the glass beads is set as 30°, which will also affect the simulation results. What's more, the roughness of the wall is also difficult to be the same as the experiment. The error of the free surface elevations may come from the mixture of the water and air. The Euler-Euler multiphase flow model is an attempt to capture the free surface elevations.

3.2. Effect of the initial depositional form of sediments (H/L)

Keeping the slope angle and the relative depth of sediments unchanged, the relationship between front velocity (U^*) and the initial depositional form of sediments (H/L) is studied (Case 1-5). Fig. 8 shows the evolution of the front velocity (U^*) with time (T) at different H/L. The front velocity increases with time at all the five cases. With the increase of H/L, the mudflow shows a noticeable increase in front velocity. The physical explanation is that when H/L is large, the sediment has a large gravitational potential energy. The mudflow is affected by the frictional resistance on the seabed and the dynamic resistance of the seawater during the mass movement. The gravitational potential energy converts into the kinetic energy in the flowing process. With a large gravitational potential energy, the front velocity of mudflow is relatively high. However, the movement pattern tends to be the same (the front velocity increases with time). It can also be found that the front velocity drops suddenly at about $T = 10$ when $H/L = 0.100$ and 0.125. The reason for this phenomenon is the frontal detachment during the mass movement which will be discussed in Section 3.3.

3.3. Formation condition of hydroplaning and frontal detachment

Hydroplaning is a thin layer of lubricating water between the submarine mudflow and the slope, which is caused by the hydrodynamic pressures deforming the wetted perimeter from the stagnation point down to the seabed. The resistance of the seawater on the submarine mudflow is $P_f = 0.5\rho_w U^2$. The mud-load is $P_s = (\rho_s - \rho_w)gh_a cos\theta$, where h_a is the average thickness of the submarine mudflow. The dimensionless Froude number prescribed by Mohrig et al. (1998) is related to P_f and P_s:

$$Fr = \sqrt{\frac{2P_f}{P_s}} = \frac{U}{\sqrt{(\rho^* - 1)gh_a cos\theta}}, \tag{28}$$

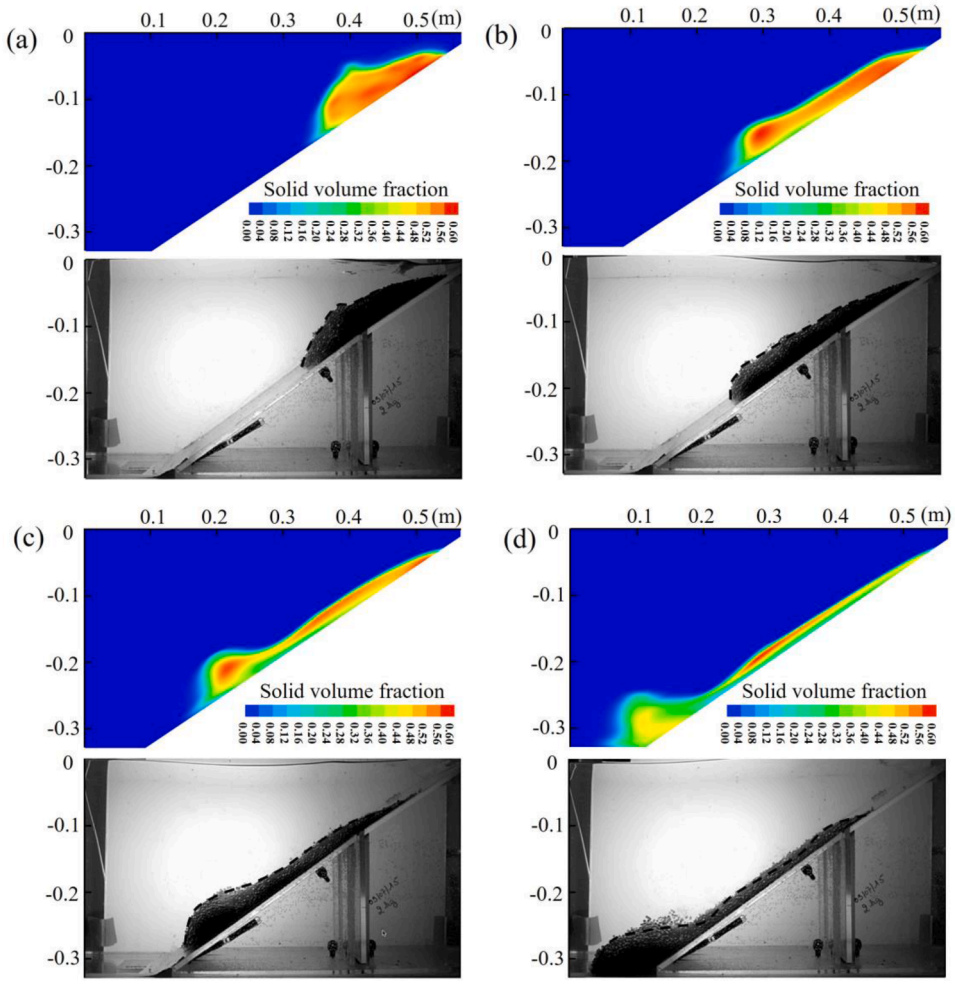

Fig. 5. Comparison of the slide cross sections between the numerical simulation results and the experimental image with high-speed video camera, at times (a) 0.17 s, (b) 0.32 s, (c) 0.47 s, and (d) 0.62 s. Color scales are computed glass volume fraction.

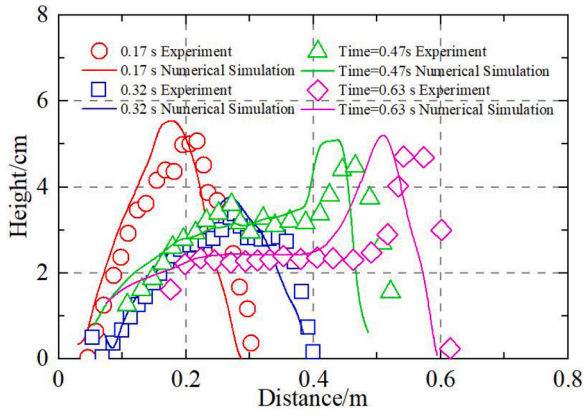

Fig. 6. Comparison of the stacking height of the glass beads between the numerical simulation results and the experimental data, at times (a) 0.17 s, (b) 0.32 s, (c) 0.47 s, and (d) 0.62 s.

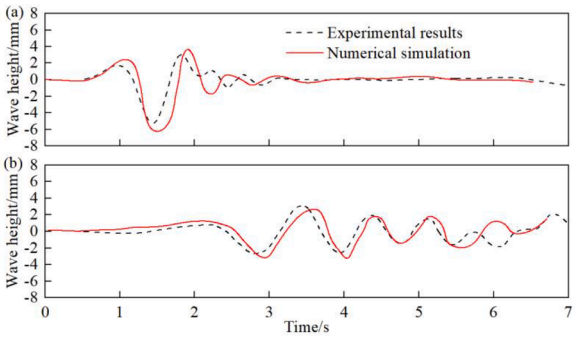

Fig. 7. Comparison of the time series of free surface elevations between the numerical simulation results and the experimental data at (a) wave gage 1, and (b) wave gage 3 in experiments of Grilli et al. (2017).

where ρ^* is the ratio of the sediment density to the seawater density. The Froude number in Eq.(28) is similar to non-dimensional front velocity (U^*) in Eq.(26). When the front velocity is small (Fr<0.3), the front resistance is also small and there is no hydroplaning during the mudflow movement. When Fr>0.4, the head of the mudflow pushes the seawater away from its path, and the dynamic pressure increases, causing the head to hydroplane. Fig. 9(a) shows the hydroplaning in the numerical simulation (Case 4), where h_a = 47 m, U = 63 m/s, and Fr = 2.2. Hydroplaning could induce the mobility by reducing the frictional resistance between the front of the mudflow and the slope, leading to long sliding distances of the mudflow.

In addition, the front part of the submarine mudflow moves fast while the rear part moves slowly. Finally, the front part gradually detaches from the main body (Fig. 9(c)). This phenomenon is also found in the existing submarine mudflow and the laboratory experiment (Ilstad

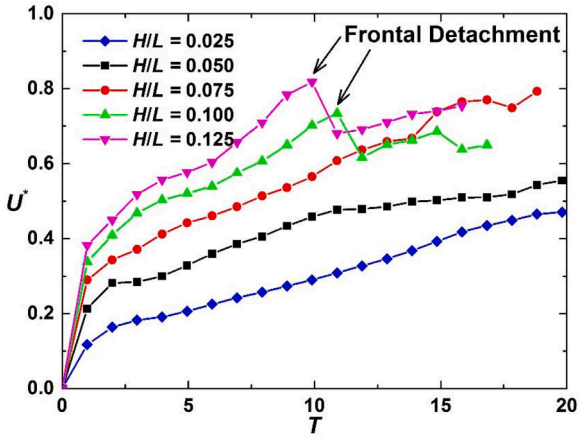

Fig. 8. The front velocity of the submarine mudflow with time at different H/L values. The five velocity curves correspond to Case1-5 in Table 2.

et al., 2004).

3.4. *Effect of the relative depth of sediments (h/L) on the seabed and the slope angle (θ)*

Fig. 10 shows the evolution of the front velocity at different values of h/L and θ. The relative depth of the submarine mudflow has little influence on the front velocity, because the h/L values mainly affect the magnitude of hydrostatic pressure on the submarine mudflow. The main forces on the submarine mudflow are the frictional resistance of the slope, dynamic resistance of the seawater, and gravity. The submarine mudflow on the seabed that occurs at different depth is affected little by the depth of seawater.

The submarine mudflow occurs frequently and can travels hundreds of kilometers on gentle slopes. The influence of the slope angle on the mudflow is clear. When the slope angle is large, the submarine mudflow is subjected to a greater sliding force. Consequently, the acceleration of the submarine mudflow increases, and the sliding distance is greater than it would be otherwise. Based on the numerical simulation results, the larger the slope angle, the larger the front velocity acceleration of the submarine mudflow and the higher the value of the front velocity.

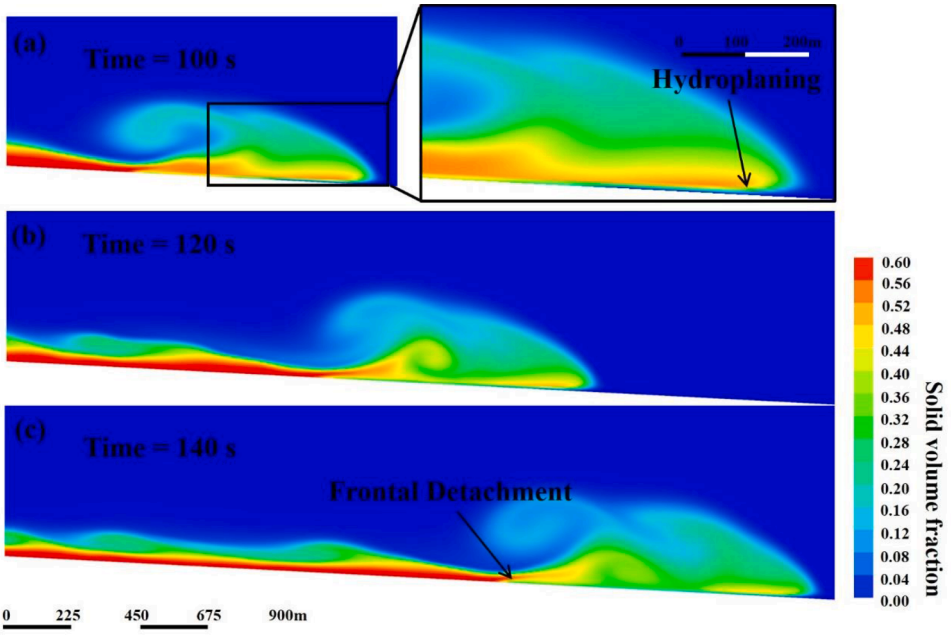

Fig. 9. Contour of the volume fraction the sediment phase, at times t (a) t = 100 s, (b) t = 120 s, and (c) t = 140 s. The black frame in contour (a) shows the hydroplaning. The frontal detachment of the mudflow appears at about 140 s where the black arrow indicates in contour (c). (Case 4 in Table 2)

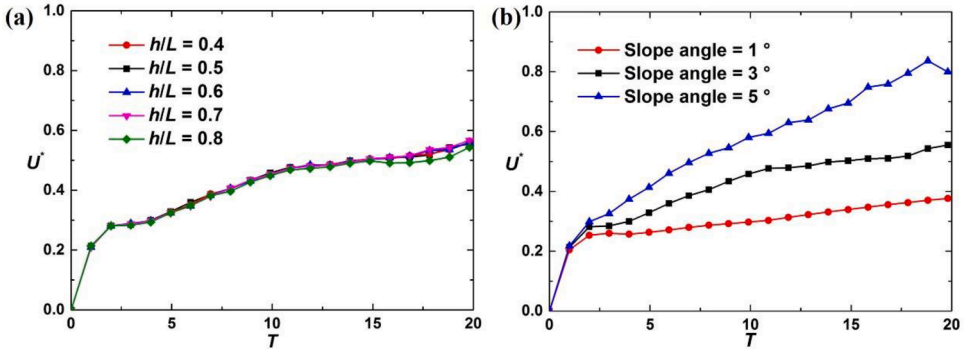

Fig. 10. Evolution of the front velocity (a) different relative depth of sediments (h/L) (b) different slope angle (θ). The five velocity curves in (a) correspond to Case 2, 6, 7, 8, and 9 in Table 2. The three velocity curves in (b) correspond to Case 2, 10, and 11 in Table 2.

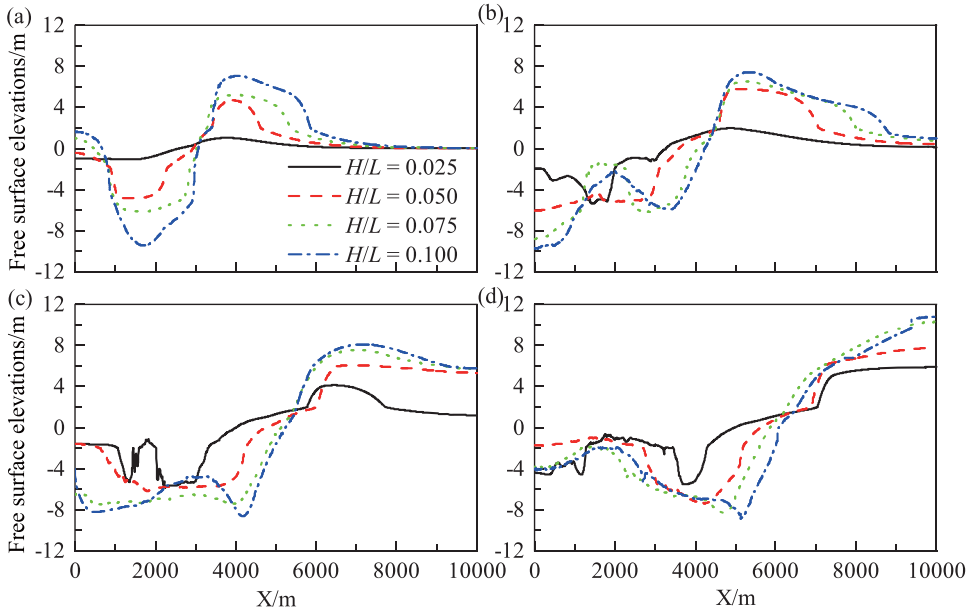

Fig. 11. The free surface elevations at the sea level with different time, t = (a) 40 s, (b) 80 s, (c) 120 s, and (d) 160 s at various values of H/L.

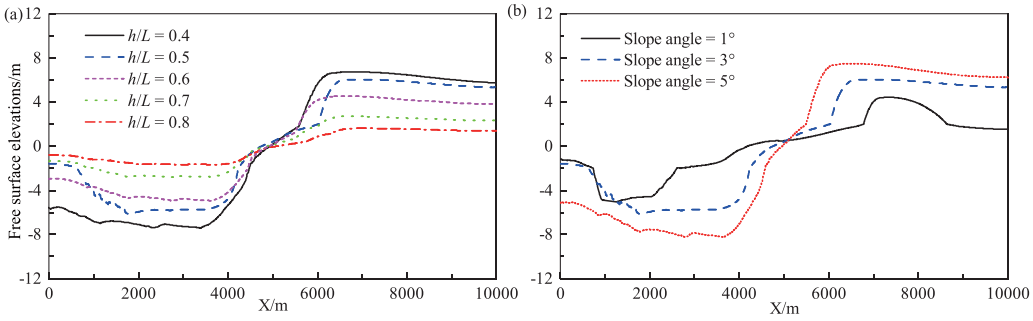

Fig. 12. The free surface elevations at time = 80 s, (a) different h/L value, (b) different slope angle θ.

3.5. Effect of the submarine mudflow on the sea level

The submarine mudflow may influence the sea level, and cause sea waves, even tsunamis. The free surface elevations at the sea level during the mass movement of the submarine mudflow are simulated and observed. In the numerical simulation, we find that the maximum value of the free surface elevations is approximately 8 m (Case 4 time = 120 s). The free surface elevations near the left and right boundaries (Fig. 1) are not considered. Fig. 11 shows the free surface elevations at the sea level with different time (t = 40 s, 80 s, 120 s, and 160 s) at various values of H/L. With the increase of the H/L value, the maximum free surface elevations increases. A large H/L value represents a great gravitational potential energy and a large kinetic energy, as well as the energy transformed into the movement of seawater. The maximum free surface elevations is positively related to the energy transformed into the seawater. As the submarine mudflow movement time increases, maximum free surface elevations position shifts to the direction of submarine mudflow movement. The evolution of free surface elevations at the sea level at different h/L value and slope angle is shown in Fig. 12. The peak value of free surface elevations at the sea level decreases with the increase of the h/L value. The deeper the submarine mudflow is from the sea level, the smaller the influence of the submarine mudflow on the sea level and the smaller the free surface elevations. With a great relative depth (large h/L), the effect of the submarine mudflow on the sea level will be small. In addition, due to the fact that the submarine mudflow on the seabed that occurs at different depths is affected little by the depth of seawater, the maximum free surface elevations position is basically the same. With the slope angle increases from 1° to 5°, the maximum free surface elevations increases from 3.8 m to 7.1 m at time 80 s. Because when the slope angle is larger, the front velocity of submarine mudflow increases. Based on the numerical simulation results, the mass movement of the submarine mudflow plays an important role in sea level fluctuations. The effect should be taken into consideration in the construction of offshore platform.

4. Conclusion

We investigate the flow characteristics of large-scale SMMM based on the Euler-Euler multiphase flow model combining with the KTGF. The values of each physical parameter refer to the previous experiments of our group and previous researchers' results. The dimensionless parameters such as the initial depositional form of the sediments (H/L), the relative depth of the submarine mudflow (h/L), and the slope angle (θ) are derived, and the effects of these controlling parameters are analyzed.

The presented model is verified by comparing the numerical results with the previous experiments. The submarine mudflow shows a noticeably increased front velocity with the increase of the H/L values. In other words, when the H/L value is larger, the submarine mudflow impact is stronger. The relative depth of the submarine mudflow (h/L) has little influence on the front velocity. The larger slope angle leads to the longer acceleration process and the higher peak value of the front velocity. The front part may detach from the main body due to the high

velocity of the front part of the submarine mudflow. With the increase of the H/L value, the maximum free surface elevations at the sea level increases. The peak value of the free surface elevations decreases with the increase of the h/L value. The maximum value of the free surface elevations is about 8 m. The submarine mudflow should be taken into consideration in the construction of offshore platform.

Author statement

No conflict of interest exits in the submission of this manuscript, and manuscript is approved by all authors for publication. I would like to declare on behalf of my co-authors that the work described was original research that has not been published previously, and not under consideration for publication elsewhere, in whole or in part. All the authors listed have approved the manuscript that is enclosed.

Declaration of Competing Interest

The authors declare that they have no known competing financial interests or personal relationships that could have appeared to influence the work reported in this paper.

Acknowledgements

This work was supported by the National Natural Science Foundation of China [grant numbers 11872365 and 51639008]; and the Youth Innovation Promotion Association of the Chinese Academy of Sciences [grant number 2017027]. We would like to thanks associate professor Yi An for the helpful suggestions and Tezhuan Du for assistance with the multiphase flow model of the submarine mudflow.

References

Abbas, Y.B., Kazeminezhad, M.H., Amir, E.S., Baas, J.H., Cheng, L., 2011. Euler–Euler two-phase flow simulation of tunnel erosion beneath marine pipelines. Appl. Ocean Res. 33, 137–146. https://doi.org/10.1016/j.apor.2011.01.001.

Brune, S., Babeyko, A.Y., Gaedicke, C., Ladage, S., 2010. Hazard assessment of underwater landslide-generated tsunamis: a case study in the Padang region, Indonesia. Nat. Hazards 53, 205–218. https://doi.org/10.1007/s11069-009-9424-x.

Cashman, K.V., Popenoe, P., 1985. Slumping and shallow faulting related to the presence of salt on the Continental Slope and Rise off North Carolina. Mar. Petrol. Geol. 2, 260–271. https://doi.org/10.1016/0264-8172(85)90016-9.

Cheng, Z., Hsu, T.J., Calantoni, J., 2017. SedFoam: A multi-dimensional Eulerian two-phase model for sediment transport and its application to momentary bed failure. Coast Eng. 119, 32–50. https://doi.org/10.1016/j.coastaleng.2016.08.007.

Chen, Y.M., Zhang, L.L., Liao, C.C., Jiang, M.J., Peng, M., 2020. A two-stage probabilistic approach for the risk assessment of submarine landslides induced by gas hydrate exploitation. Appl. Ocean Res. 99, 102158 https://doi.org/10.1016/j.apor.2020.102158.

De Blasio, F.V., Elverhoi, A., Issler, D., Bryn, P., Lien, R., 2004. Flow models of natural debris flows originating from overconsolidated clay materials. Mar. Geol. 213, 439–455. https://doi.org/10.1016/j.margeo.2004.10.018.

Dillon, W.P., Danforth, W., Hutchinson, D.R., Drury, R.M., Taylor, M.H., Booth, J.S., 1998. Evidence for faulting related to dissociation of gas hydrate and release of methane off the southeastern United States. Geol. Soc. Lond. Spec. Publications 137, 293–302. https://doi.org/10.1144/GSL.SP.1998.137.01.23.

Ding, J., Gidaspow, D., 1990. A bubbling fluidization model using kinetic theory of granular flow. AIChE J. 36, 523–538. https://doi.org/10.1002/aic.690360404.

Dong, Y., Wang, D., Randolph, M.F., 2017. Runout of submarine landslide simulated with material point method. J. Hydrodyn. 29, 438–444. https://doi.org/10.1016/S1001-6058(16)60754-0.

Gauer, P., Elverhoi, A., Issler, D., De Blasio, F.V., 2006. On numerical simulations of subaqueous slides: back-calculations of laboratory experiments of clay-rich slides. Norw. J. Geol. 86, 295–300.

Gidaspow, D., Bezburuah, R., Ding, J., 1991. Hydrodynamics of circulating fluidized beds: kinetic theory approach. In: 7th International Conference on Fluidization. Gold Coast, Australia.

Gidaspow, D., 1994. Multiphase Flow and Fluidization: Continuum and Kinetic Theory Descriptions, first ed. Academic Press, Boston.

Guo, X.S., Zheng, D.F., Nian, T.K., Yin, P., 2019. Effect of different span heights on the pipeline impact forces induced by deep-sea landslides. Appl. Ocean Res. 87, 38–46. https://doi.org/10.1016/j.apor.2019.03.009.

Grilli, S.T., Shelby, M., Kimmoun, O., Dupont, G., Nicolsky, D., Ma, G.F., Kirby, J.T., Shi, F.Y., 2017. Modeling coastal tsunami hazard from submarine mass failures: effect of slide rheology, experimental validation, and case studies off the US East Coast. Nat. Hazards 86, 353–391. https://doi.org/10.1007/s11069-016-2692-3.

Haza, Z.F., Harahap, I.S.H., Dakssa, L.M., 2013. Experimental studies of the flow-front and drag forces exerted by subaqueous mudflow on inclined base. Nat. Hazards 68, 587–611. https://doi.org/10.1007/s11069-013-0643-9.

Ilstad, T., Marr, J.G., Elverhoi, A., Harbitz, C.B., 2004. Laboratory studies of subaqueous debris flows by measurements of pore-fluid pressure and total stress. Mar. Geol. 213, 403–414. https://doi.org/10.1016/j.margeo.2004.10.016.

Jiang, M.J., Chao, S., Giovanni, B.C., Zhang, W.C., 2015. A study of submarine steep slope failures triggered by thermal dissociation of methane hydrates using a coupled CFD-DEM approach. Eng. Geol. 190, 1–16. https://doi.org/10.1016/j.enggeo.2015.02.007.

Johnson, P., Jackson, R., 1987. Frictional-collisional constitutive relations for granular materials, with application to plane shearing. J. Fluid Mech. 176, 67–93. https://doi.org/10.1017/S0022112087000570.

Lee, C.H., Huang, Z.H., Chiew, Y.M., 2015. A three-dimensional continuum model incorporating static and kinetic effects for granular flows with applications to collapse of a two-dimensional granular column. Phys. Fluids 27, 113303. https://doi.org/10.1063/1.4935626.

Lee, C.H., 2019. Multi-phase flow modeling of submarine landslides: transformation from hyperconcentrated flows into turbidity currents. Adv. Water Resour. 131, 103383 https://doi.org/10.1016/j.advwatres.2019.103383.

Li, G., George, J.M., Zhang, K., Li, X.S., 2010. Evaluation of gas production potential from marine gas hydrate deposits in Shenhu Area of South China Sea. Energy Fuels 24, 6018–6033. https://doi.org/10.1021/ef100930m.

Li, L.L., Adam, D.S., Wang, Y., Weiss, R., Qiu, Q., Chan, Q.H., Tapponnier, P., 2015. What caused the mysterious eighteenth century tsunami that struck the southwest Taiwan coast? Geophys. Res. Lett. 42, 8498–8506. https://doi.org/10.1002/2015gl065567.

Liu, F., Wu, S., Sun, Y., 2010. A quantitative analysis for submarine slope instability of the northern South China Sea due to gas hydrate dissociation. Chin. J. Geophys. 53, 946–953 in Chinese.

Locat, J., Lee, H.J., 2002. Submarine landslides: advances and challenges. Can. Geotech. J. 39, 193–212. https://doi.org/10.1139/t01-089.

Lun, C.K.K., Savage, S.B., Jeffrey, D.J., Chepurniy, N., 1984. Kinetic theories for granular flow: inelastic particles in Couette flow and slightly inelastic particles in a general flowfield. J. Fluid Mech. 140, 223–256. https://doi.org/10.1017/S0022112084000586.

Lu, X.B., Chen, X.D., Lu, L., Zhang, X.H., 2017. Numerical simulation on the marine landslide due to gas hydrate dissociation. Environ. Earth. Sci. 6, 172. https://doi.org/10.1007/s12665-017-6477-0.

Mosher, D.C., Moscardelli, L., Shipp, R.C., Chaytor, J.D., Baxter, C.D.P., Lee, H.J., Urgeles, R., 2010. Submarine Mass Movements and Their Consequences, first ed. Springer, Dordrecht. https://doi.org/10.1007/978-90-481-3071-9_1.

Mohrig, D., Elverhoi, A., Parker, G., 1999. Experiments on the relative mobility of muddy subaqueous and subaerial debris flows, and their capacity to remobilize antecedent deposits. Mar. Geol. 154, 117–129. https://doi.org/10.1016/s0025-3227(98)00107-8.

Mohrig, D., Whipple, K.X., Hondzo, M., Ellis, C., Parker, G., 1998. Hydroplaning of subaqueous debris flows. Geol. Soc. Am. Bull. 110, 387–394, 10.1130/0016-7606(1998)110≤0387:hosdf≥2.3.co;2.

Ogawa, S., Umemura, A., Oshima, N., 1980. On the equations of fully fluidized granular materials. Zeitschrift für angewandte Mathematik und Physik 31, 483–493. https://doi.org/10.1007/bf01590859.

Qiu, L.C., Jin, F., Lin, P.Z., Liu, Y., Han, Y., 2017. Numerical simulation of submarine landslide tsunamis using particle based methods. J. Hydrodyn. 29, 542–551. https://doi.org/10.1016/s1001-6058(16)60767-9.

Schaeffer, D.G., 1987. Instability in the evolution equations describing incompressible granular flow. J. Differ. Equ, 66, 19–50. https://doi.org/10.1016/0022-0396(87)90038-6.

Si, P.F., Shi, H.B., Yu, X.P., 2018. Development of a mathematical model for submarine granular flows. Phys. Fluids 30, 083302. https://doi.org/10.1063/1.5030349.

Su, Z., George, J.M., Zhang, K., Wu, N.Y., 2012. A huff-and-puff production of gas hydrate deposits in Shenhu area of South China Sea through a vertical well. J. Petrol. Sci. Eng. 86-87, 54–61. https://doi.org/10.1016/j.petrol.2012.03.020.

Syamlal, M., Rogers, W., O'Brien, T.J., 1993. MFIX Documentation Theory Guide. National Technical Information Service, Springfield, United States.

Tan, Q.M., 2011. Dimensional analysis: with Case Studies in Mechanics, first ed. Springer, Berlin. https://doi.org/10.1007/978-3-642-19234-0.

Terry, J.P., Nigel, W., James, G., Tan, P.H.H., 2017. Past and potential tsunami sources in the South China Sea: a brief synthesis. Earth-Sci. Rev. 167, 47–61. https://doi.org/10.1016/j.earscirev.2017.02.007.

Vanneste, M., Sultan, N., Garziglia, S., Forsberg, C.F., L'Heureux, J.S., 2014. Seafloor instabilities and sediment deformation processes: the need for integrated, multi-disciplinary investigations. Mar. Geol. 352, 183–214. https://doi.org/10.1016/j.margeo.2014.01.005.

Wang, X.J., Deborah, R.H., Wu, S.G., Yang, S.X., Guo, Y.Q., 2011. Elevated gas hydrate saturation within silt and silty clay sediments in the Shenhu area, South China Sea. J. Geophys. Res. 116, B05102. https://doi.org/10.1029/2010jb007944.

Wang, X.J., Timothy, S.C., Myung, W.L., Yang, S.X., Guo, Y.Q., Wu, S.G., 2014. Geological controls on the occurrence of gas hydrate from core, downhole log, and seismic data in the Shenhu area, South China Sea. Mar. Geol. 357, 272–292. https://doi.org/10.1016/j.margeo.2014.09.040.

Wu, N.Y., Zhang, H.Q., Yang, S.X., Zhang, G.Q., Liang, J.Q., Lu, J.A., Su, X., Schultheiss, P., Holland, M., Zhu, Y.H., 2011. Gas hydrate system of Shenhu area, Northern South China Sea: geochemical results. J. Geol. Res., 370298 https://doi.org/10.1155/2011/370298.

Xiu, Z.X., Liu, L.J., Xie, Q.H., Li, X.S., Hu, G.H., Li, J.G., Zhao, Q., 2016. Sensitivity analysis of submarine landslide mass movement based on the small-scale numerical model. Mar. Sci. Bull. 35, 380–385 in Chinese.

Xiu, Z.X., Liu, L.J., Xie, Q.H., Li, J.G., Hu, G.H., Yang, J.H., 2015. Runout prediction and dynamic characteristic analysis of a potential submarine landslide in Liwan 3-1 gas field. Acta Oceanol. Sin. 34, 116–122. https://doi.org/10.1007/s13131-015-0697-2.

Yu, M.L., Lee, C.H., 2019. Multi-phase-flow modeling of underwater landslides on an inclined plane and consequently generated waves. Adv. Water Resour. 33, 103421 https://doi.org/10.1016/j.advwatres.2019.103421.

Zakeri, A., Hoeg, K., Nadim, F., 2009. Submarine debris flow impact on pipelines - Part II: numerical analysis. Coast Eng. 56, 1–10. https://doi.org/10.1016/j.coastaleng.2008.06.005.

Zakeri, A., 2009. Submarine debris flow impact on suspended (free-span) pipelines: normal and longitudinal drag forces. Ocean Eng. 36, 489–499. https://doi.org/10.1016/j.oceaneng.2009.01.018.

Zhang, W., Liang, J.Q., Lu, J., Wei, J.Q., Su, P.B., Fang, Y.X., Guo, Y.Q., Yang, S.X., Zhang, G.X., 2017. Accumulation features and mechanisms of high saturation natural gas hydrate in Shenhu Area, northern South China Sea. Petrol. Explor. Dev. 44, 708–719. https://doi.org/10.1016/S1876-3804(17)30082-4.

Zhang, W., Liang, J.Q., Wei, J.G., Lu, J.A., Su, P.B., Lin, L., Huang, W., Guo, Y.Q., Deng, W., Yang, X.L., Wan, Z.F., 2020. Geological and geophysical features of and controls on occurrence and accumulation of gas hydrates in the first offshore gas-hydrate production test region in the Shenhu area, Northern South China Sea. Mar. Petrol. Geol. 114, 104191 https://doi.org/10.1016/j.marpetgeo.2019.104191.

Zhang, X.H., Lu, X.B., Shi, Y.H., Xia, Z., 2015. Study on the mechanical properties of hydrate-bearing silty clay. Mar. Petrol. Geol. 67, 72–80. https://doi.org/10.1016/j.marpetgeo.2015.04.019.

Zhang, Y., Wang, Z.T., Yang, Q., Wang, H.Y., 2019. Numerical analysis of the impact forces exerted by submarine landslides on pipelines. Appl. Ocean Res. 92, 101936 https://doi.org/10.1016/j.apor.2019.101936.